Electrochimica Acta 343 (2020) 136070

Contents lists available at ScienceDirect

Electrochimica Acta

journal homepage: www.elsevier.com/locate/electacta

# A novel quantitative electrochemical aging model considering side reactions for lithium-ion batteries

Xi Zhang [a, *], Yizhao Gao [a], Bangjun Guo [a], Chong Zhu [a], Xuan Zhou [b], Lin Wang [c], Jianhua Cao [c]

[a] School of Mechanical Engineering, Shanghai Jiao Tong University, Shanghai, China
[b] Department of Electrical and Computer Engineering, Kettering University, MI, USA
[c] Shanghai E Propulsion Auto Technology Co., Ltd, Shanghai, China

ARTICLE INFO

*Article history:*
Received 10 November 2019
Received in revised form
11 March 2020
Accepted 13 March 2020
Available online 16 March 2020

*Keywords:*
Lithium-ion batteries
Quantitative electrochemical aging model
Side reactions
Transfer-function type
Post-mortem analysis
Macroscopic and microscopic validation

ABSTRACT

A novel quantitative electrochemical aging model for lithium-ion batteries considering side reactions is proposed in this paper. The resistance of solid electrolyte interphase and the thickness of deposited layer caused by side reactions are utilized as degradation representatives to explicitly quantify the aging effects. The aging model is established through deriving the transfer function relationship between the aging representatives and input current history. Therefore, the gap between macroscopic (battery operating mode) and microscopic (aging mechanism) can be well bridged. The aging mechanisms for the lithium-ion batteries are well identified by comprehensive post-mortem analysis. The experimental results demonstrate that the irreversible side reactions occurring at the surface of anode particles are the primary cause for performance degradation in this study. To verify the proposed aging model, the comparisons are made between experimental and simulated results at both macroscopic cell-level (cell voltage response, capacity fade, and solid-electrolyte interphase resistance increase) and microscopic-level (deposited-layer growth). The capacity decay error is bounded to 3% up to 400 cycles. The results demonstrate that the presented transfer-function type aging model is capable of predicting battery degradation severity precisely.



## 1. Introduction

### 1.1. Motivation and challenges

Lithium-ion (Li-ion) batteries have dominated the market share of power storage in electric vehicles (EVs), hybrid electric vehicles (HEVs) and plug-in hybrid vehicles (PHEVs) in recent years due to their improved energy and power densities compared to previous battery chemistries [1]. Long cell lifetime is one of the key performances ensuring EVs' popularization [2]. However, battery aging has become a critical issue for long lifespan required by automobile applications [3]. The resistance growth and the capacity fade are two immediate consequences evoked by aging process [5]. The aim to strengthen battery performances stimulates the need for a better understanding of battery aging mechanism.

Identifying degradation mechanisms in a battery is a challenging goal. When a cell is being cycled, various aging processes take place as a function of operating conditions and environmental factors, which makes modelling the battery aging effects a difficult task [6]. Therefore, this motivates us to investigate the intrinsic battery aging mechanism thoroughly and establish a quantitative analysis of the aging phenomenon.

### 1.2. Literature review

In recent years, many researchers have made considerable efforts to explore the battery aging through experiments and theoretical/numerical studies. The side reactions leading to the solid electrolyte interphase (SEI) growth at anode are assumed to be the main contributor to capacity and power fade [10]. [32] When a battery is being charged, the low potential difference between electrode and electrolyte at the anode is inductive to side reactions [8]. The growth of SEI consumes the electrolyte and recyclable $Li^+$ to form a deposited layer on the anode particle surface [9]. Due to

* Corresponding author. School of Mechanical Engineering, Shanghai Jiao Tong University, Shanghai, China.
*E-mail address:* braver1980@sjtu.edu.cn (X. Zhang).

https://doi.org/10.1016/j.electacta.2020.136070
0013-4686/

poor ionic conductivity of the deposit, the overgrowth of SEI film increases internal resistance and power fade [7]. By performing post-mortem analysis on aged cells, it is found that the SEI displays uneven distribution characteristics on the anode particle surface [11]. Moreover, the growth rate of SEI could be accelerated by raising the cycling SOC range [12] or elevating temperatures [13]. Large heat evolution during high current charge-discharge also has a significant impact on battery degradation process [14]. Although they provided valuable insights into battery aging, no corresponding mathematical models were established to quantify these side reactions. Given that the SEI aging process often couples with the cell electrochemistry, aging quantitative analysis requires an accurate electrochemical battery model. Complex full-order physics-based models are characterized by a series of highly nonlinear partial differential equations (PDEs), which demand massive computation resources [15]. Equivalent circuit models [3] are able to reduce the computation burden but require tremendous empirical parametrizations, and lack the exploration of underlying physical process [9]. The simplified electrochemical models integrated with the battery internal mechanisms provide another way to obtain the desired computational performances. In this regard, an averaged physics-based single particle model (SPM) with SEI induced capacity fade was formulated but may not applicable for high C-rates [16]. The electrolyte enhanced single particle model (eSPM) was further simplified to obtain an analytical aging formula considering SEI growth [6]. By using the finite analysis method and numerical computation method, five aging characteristic parameters were extracted and the aging trajectories at different temperatures were built [4]. A capacity degradation model with dynamic load based on mechanistic and prognostic principles including SEI growth was presented [5]. In Ref. [17], the capacity loss due to SEI growth and isolation of active material were accurately described by a computationally efficient degradation model for Li-ion battery graphite anodes. Similarly, the mechanism of porosity modification due to SEI growth at anode was integrated to formulate an isothermal physics-based model [18]. The physics-based PDEs were discretized step by step and approximated to obtain a control-oriented incremental aging model [19]. Through dividing the SEI growth process into two linearly combined parts: one stemming from parts of particles covered by SEI and one contribution from parts of the particles were the SEI layer cracked due to graphite expansion, an aging model for moderate currents up to 1C was derived [20]. The cubic polynomial functions were used for approximating the electrolyte concentration and potential inside electrodes in developing a reduced-order aging model [21]. The pore clogging [22] or electrolyte depletion due to side reactions [23] were assumed to cause the capacity decay from linear to nonlinear. The temperature and variable porosity effects on battery aging were analyzed in detail [24]. Transfer-function mathematical model is a visualized tool in depicting the relationship between input current and battery electrochemical variables, which could be constructed in Simulink directly. This is helpful to produce the real-time codes to a battery management system (BMS) [25]. However, the battery aging dynamics are not included [26]. To fully address the gap between battery usage history (macro-) and aging degradation mechanism (micro-), the aging model should not only consider cells' external dynamic responses (voltage, capacity), but also provide the solid physical evidence for battery internal degradation mechanisms.

Developing an accurate control-oriented aging model is essential for an advanced BMS. For instance, such a model can be applied to health-aware fast charging protocol [37], fault diagnosis [38], and available power prediction [39]. Moreover, to obtain a precise electrochemical aging model, the mathematical relationship between input current history and battery degradation representatives should be systematically validated through comprehensive physical analysis at both macroscopic and microscopic levels.

### 1.3. Novelty and main contributions

In this paper, a novel simplified transfer-function type electrochemical aging model considering side reactions is proposed and verified. Growth of deposited layer and SEI resistance are selected as degradation representatives to quantify the battery aging effects. The mathematical relationship between these degradation representatives and input current is established to form a simplified transfer-function type aging model. To verify the proposed model, the battery's voltage response, capacity decay and SEI resistance growth are first utilized to validate the aging model at cell level. Then the degradation mechanism for cycled cells is identified thoroughly via comprehensive post-mortem analysis. The experimental results elucidate that the side reactions at anode are the major cause for performance decay. Based on these observations, the thickness of the deposited layers are measured and compared to the simulated results to validate the correctness and effectiveness of the aging model microscopically. The loss of electrolyte and active materials due to side reactions over cycling are also considered. To the best of the author's knowledge, it is the first time that the transfer-function relationship between battery degradation and battery input current history is directly formulated and validated thoroughly, which provides a brand-new insight into battery aging comprehension. In addition, the gap between battery mathematical modelling and degradation mechanism investigation could be well bridged.

### 1.4. Paper organization

This paper is organized as follows. In section 2, the electrochemical aging model is established. The overall experimental procedures are introduced in section 3. The experimental and simulated results are analyzed in section 4 for model verification. The conclusion is drawn in section 5.

## 2. Electrochemical-aging model establishment

As shown in Fig. 1, the Li-ion battery is assumed to be constructed by two electrodes composed of a large number of uniform radius balls and the separator. In the positive and negative electrodes, the active materials are oxidized or reduced, and meanwhile the Li ions are de-intercalated from or intercalated to the electrode and migrated through the electrolyte. The particle radius of the active materials is defined as $R$. The parameters are assumed to change only in the direction of $x$, and $L$ denotes the distance between the negative and positive electrode in the battery [25]. The potentials or concentrations are related to the $x$ position. When side reactions occur at the interface between the electrode particles and the electrolyte, the reaction products stick to the surface of the anode particles to cause the over-growth of SEI and then form a deposited layer at the interface between the anode and the separator [7]. The deposits can clog the pores of the particles that decrease the effective surface of the active materials. Finally, a portion of the particles covered by the deposits are electrically isolated and unable to participate in chemical reaction anymore [34].

The $Li^+$ diffusion in the solid is assumed to follow:

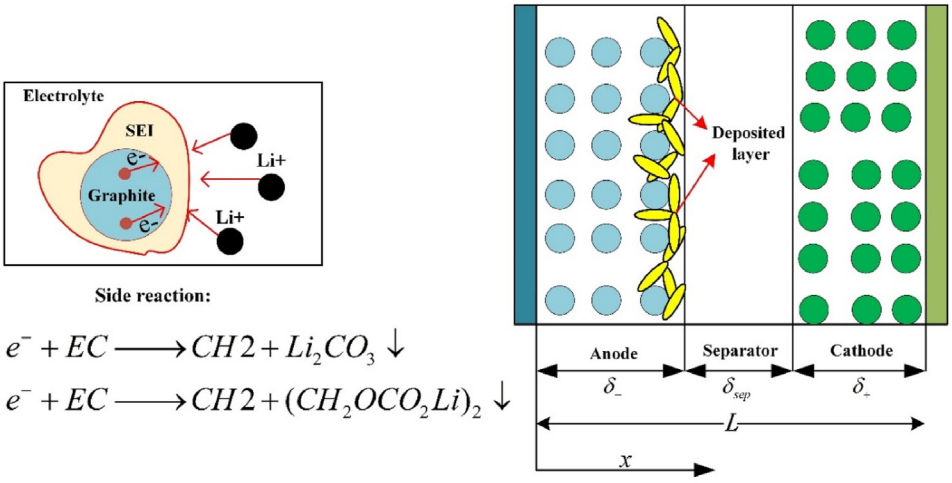


**Fig. 1.** Schematic diagram of the lithium-ion battery.

$$\frac{\partial c_s}{\partial t} = \frac{D_s}{r^2}\frac{\partial}{\partial r}\left(r^2\frac{\partial c_s}{\partial r}\right) \tag{1}$$

The boundary conditions are:

$$\left.\frac{\partial c_s}{\partial r}\right|_{r=0} = 0, D_s\left.\frac{\partial c_s}{\partial r}\right|_{r=R_s} = -\frac{j}{F}$$

where $j$ denotes the reaction flux across the boundary of the solid.

Concentration of $Li^+$ in the electrolyte $c_e$ is described as:

$$\varepsilon_e\frac{\partial c_e}{\partial t} = D_e^{eff}\frac{\partial^2 c_e}{\partial x^2} + \frac{a_s(1-t_+^0)}{F}j \tag{2}$$

where the boundary conditions are given by:

$$\left.\frac{\partial c_e}{\partial x}\right|_{x=0} = \left.\frac{\partial c_e}{\partial x}\right|_{x=L} = 0$$

Conservation of charge in the solid phase produces the governing equation for the potential in the solid phase

$$\sigma^{eff}\frac{\partial^2\varphi_s}{\partial x^2} - a_s j = 0 \tag{3}$$

with boundary conditions:

$$-\sigma_-^{eff}\left.\frac{\partial\varphi_s}{\partial x}\right|_{x=0} = \sigma_+^{eff}\left.\frac{\partial\varphi_s}{\partial x}\right|_{x=L} = \left.\frac{I}{A}\frac{\partial\varphi_s}{\partial x}\right|_{x=\delta_-} = \left.\frac{\partial\varphi_s}{\partial x}\right|_{x=\delta_-+\delta_{sep}} = 0$$

Conservation of charge in the electrolyte phase gives the equation for the potential of the electrolyte phase

$$k^{eff}\frac{\partial^2\varphi_e}{\partial x^2} + k_d^{eff}\frac{\partial^2 \ln c_e}{\partial x^2} + a_s j = 0 \tag{4}$$

with boundary conditions:

$$\left.\frac{\partial\varphi_e}{\partial x}\right|_{x=0} = \left.\frac{\partial\varphi_e}{\partial x}\right|_{x=L} = 0, \left.\left(k^{eff}\frac{\partial\varphi_e}{\partial x} + k_d^{eff}\frac{\partial c_e}{\partial x}\right)\right|_{x_-} = \left.\left(k^{eff}\frac{\partial\varphi_e}{\partial x} + k_d^{eff}\frac{\partial c_e}{\partial x}\right)\right|_{x_+}$$

The electrochemical kinetics are controlled by the Butler-Volmer equation:

$$j = i_0\left(\exp\left(\frac{\alpha_a F}{RT}\eta\right) - \exp\left(-\frac{\alpha_c F}{RT}\eta\right)\right) \tag{5}$$

### 2.1. Model simplification

Referring to Eq. (1) combined with boundary conditions and utilizing the Laplace transform gives a transcendental transfer function between the surface solid phase concentration and the current density [24]. By discretizing the transcendental transfer function via a 2nd order Pade approximation, the following simplified expressions are obtained [26]:

$$\frac{\tilde{C}_{ss}(s)}{J^{Li}(s)} = -\frac{\frac{3}{FR_s} + \frac{2R_s s}{7D_s F}}{a_s\left(s + \frac{R_s^2 s^2}{35D_s}\right)} \tag{6}$$

where $a_s$ is specific interfacial area, $F$ is Faraday constant, and $D_s$ is solid phase $Li^+$ diffusion coefficient.

The intercalation current density at the negative and positive electrodes are assumed to be proportional to the input current:

$$J_n(s) = \frac{I(s)}{AF\delta_- a_s} \tag{7}$$

$$J_p(s) = -\frac{I(s)}{AF\delta_+ a_s} \tag{8}$$

where $A$ is electrode area, $\delta_{-/+}$ is the thickness of negative electrode or positive electrode.

The governing Eq. (4) for electrolyte concentration is solved at three domains-anode, separator and cathode, respectively. At each domain, the partial differential equation is simplified into ordinary differential equation [25]. With the Laplace transformation and Pade approximation, we obtain the transfer function between the electrolyte concentration and the input current [41]:

$$\frac{C_e(L,s)}{J_p(s)}=\frac{1}{\frac{\varepsilon_{ep}\delta_+\left(12\delta_{sep}^2+12\delta_{sep}\delta_-+3\delta_-^2+8\delta_{sep}\delta_++4\delta_-\delta_++3\delta_+^2\right)}{3\left(2\delta_{sep}+\delta_-+\delta_+\right)^2}s+\frac{4D_{e,pos}^{eff}}{\left(2\delta_{sep}\delta_++\delta_-\delta_++\delta_+^2\right)}} \tag{9}$$

$$\frac{C_e(0,s)}{J_n(s)}=\frac{1}{\frac{\varepsilon_{en}\delta_-\left(12\delta_{sep}^2+12\delta_{sep}\delta_++3\delta_-^2+8\delta_{sep}\delta_-+4\delta_-\delta_++3\delta_+^2\right)}{3\left(2\delta_{sep}+\delta_-+\delta_+\right)^2}s+\frac{4D_{e,neg}^{eff}}{\left(2\delta_{sep}\delta_++\delta_-\delta_++\delta_-^2\right)}} \tag{10}$$

where $D_e^{eff}=D_e\varepsilon_e^{1.5}$ is the effective electrolyte diffusion coefficient. The electrolyte potential can be calculated by deriving the Laplace transform of Eq. (4) with the boundary conditions:

$$\frac{\tilde{\Phi}_e(L,s)}{J_p^n(s)}-\frac{\tilde{\Phi}_e(0,s)}{J_n^n(s)}=\frac{2RT\left(1-t_+^0\right)}{c_{e,0}F}\left(\frac{C_e(L,s)}{J_p^n(s)}-\frac{C_e(0,s)}{J_n^n(s)}\right) \tag{11}$$

Applying the Laplace transform to Eq. (5) and the Taylor expression $e^x=1+x+o(x)$ produce the following expression between the intercalation current density and overpotential [7]: Here it is assumed that the truncation error $o(x)$ could not have a significant impact on the model precision and the overpotential is very small compared with the cell terminal voltage.

$$\eta_n(s)=\frac{RT}{Fi_0(\alpha_a+\alpha_c)}J_n(s) \tag{12}$$

$$\eta_p(s)=\frac{RT}{Fi_0(\alpha_a+\alpha_c)}J_p(s) \tag{13}$$

where $\alpha_a$ and $\alpha_c$ represent symmetric anodic and cathodic reaction charge transfer coefficient, respectively. $i_0=k(C_e)^{\alpha_a}(C_{s,\max}-C_{ss})^{\alpha_a}(C_{s,\max}-C_{ss})^{\alpha_c}$.

Based on the above simplified equations, the cell voltage is calculated as:

$$V_{cell}(s)=\left(U_p\left(\frac{C_{ss,p}(s)}{C_{s,p,\max}}\right)-U_n\left(\frac{C_{ss,n}(s)}{C_{s,n,\max}}\right)\right)+\left(\eta_p(s)-\eta_n(s)\right)+\left(\tilde{\Phi}_e(L,s)-\tilde{\Phi}_e(0,s)\right)-R_fI(s) \tag{14}$$

where $U_p$ and $U_n$ are the open circuit voltage of positive and negative electrode, respectively. They are functions of surface solid concentration. $R_f$ is the battery internal resistance.

Before developing a degradation model, the following assumptions are made in this paper:

- Electrode volume change, structure deformation and particle cracks caused by internal mechanical stress are not considered and modelled in this work.
- The cathode aging process and its effects on battery overall performances are neglected.
- No overcharge or undercharge is considered.

### 2.2. Aging formula considering side reactions

The desired intercalation current density is represented as $j_{int}$. When side reactions $j_{side}$ take place at the interface between the electrode particles and the electrolyte, the growth of SEI is induced as shown in Eq. (15) [10].

$$S+2Li^++2e^-\longrightarrow P \tag{15}$$

where S denotes lithium ions and the solvent of electrolyte, and P denotes the product deposited at the anode. The total volumetric current density $j_{total}$ is the sum of the current of the above two reactions:

$$j_{total}=j_{\text{int}}+j_{side} \tag{16}$$

To save computational time, the local current density of side reactions is calculated by the linearized expression as follows:

$$j_{side}=\frac{\mathrm{i}_{0,side}\alpha_{c,side}n_{side}F}{RT}\eta_{side} \tag{17}$$

where $i_{side}$ is the exchange current density of side reactions and $n_{side}$ is the number of ions involved in side reactions. Overpotential of side reactions $\eta_{side}$ is described as:

$$\eta_{\text{side}}=\varphi_s-\varphi_e-U_{eq,side}-\frac{j_n^{Li}}{a_s^n}R_{SEI} \tag{18}$$

where $U_{eq,side}$ is the equilibrium potential of side reactions.

The loss of ions consumed by side reaction $Q_{ionloss}$ is defined as the integration of the side reaction rate over the volume of composite anode with time:

$$Q_{ionloss}(\tau)=-\int_{x=0}^{\delta_-}\left(\int_{t=0}^{\tau}j_{side}(x,t)a_sdt\right)Adx \tag{19}$$

where $\delta_-$ denotes the thickness of composite anode (m), $\tau$ is the total operating time (s), $A$ is the electrode plate area, and $a_s$ is active surface area per electrode unit volume [24]. The resistance of SEI and deposit layer are defined as [7]:

$$R_{SEI}(\tau,x)=\frac{\tilde{V}_{SEI}}{k_{SEI}n_{side}F}\int_{t=0}^{\tau}j_{side}(x,t)a_sdt \tag{20a}$$

$$\delta_{DL}=\frac{\tilde{V}_{DL}}{n_{side}F}\int_{t=0}^{\tau}j_{side,x=\delta_-}a_sdt \tag{20b}$$

From Eq. (5) and Eq. (18), we can observe the coupled nature of the SEI aging and electrochemical intercalation models. Moreover, a new expression for side reaction overpotential is obtained:

$$\eta_{side}=\eta_n+U_n\left(c_{ss,n}\right)-U_{eq,side} \tag{21}$$

Linearizing the open circuit voltage of negative electrode via Taylor expansion at equilibrium produces:

$$U_n\left(c_{ss,n}\right)=U_{n,eq}+\frac{\partial U_n}{\partial c_{ss,n}}\tilde{c}_{ss,n}(t) \tag{22}$$

where $U_{n,eq}$ is the open circuit voltage at equilibrium. $\tilde{c}_{ss,n}=c_{ss,n}-c_{ss,n}^{eq}$ and $c_{ss,n}^{eq}$ indicates the average concentration at equilibrium SOC. Substituting Eq. (22) into Eq. (21) and simplifying:

$$\eta_{side}=\eta_n+C_1\tilde{c}_{ss,n}(t)+C_2 \tag{23}$$

where tilde represents the minor perturbation from the equilibrium state, $C_1=\frac{\partial U_n}{\partial c_{ss,n}}$, $C_2=U_{n,eq}-U_{eq,side}$. To exclude the influence of constant on model simplification, we assume that the open

circuit voltage expression is linearized at the equilibrium point where $U_{n,eq} = U_{eq,side}$, which sets $C_2$ to zero.

With the Laplace transformation of Eq. (21), we obtain the transfer function of side reaction potential over input current:

$$\frac{\eta_{side}(s)}{J_n(s)} = \frac{\eta_n(s)}{J_n(s)} + C_1 \frac{\tilde{c}_{ss,n}(s)}{J_n(s)} \tag{24}$$

$$\frac{\eta_{side}(s)}{J_n(s)} = \frac{RT}{Fi_0(\alpha_a + \alpha_c)} - C_1 \frac{\frac{3}{FR_s} + \frac{2R_s s}{7D_s F}}{a_s\left(s + \frac{R_s^2 s^2}{35D_s}\right)} \tag{25}$$

Substituting Eq. (25) into Eq. (17) and applying Laplace transformation gives the transfer function of side reaction rate over input current density:

$$\frac{j_{side}(s)}{J_n(s)} = \frac{i_{0,side}\alpha_{c,side}n_{side}F}{RT}\left(\frac{RT}{Fi_0(\alpha_a + \alpha_c)} - C_1 \frac{\frac{3}{FR_s} + \frac{2R_s s}{7D_s F}}{a_s\left(s + \frac{R_s^2 s^2}{35D_s}\right)}\right) \tag{26}$$

Substituting Eq. (26) into Eq. (19), Eq. (20a) and Eq. (20b) with Laplace transformation derive the transfer function of loss of ions, SEI resistance growth, and deposited layer growth over input current density, respectively:

$$\frac{Q_{ionloss}(s)}{J_n(s)} = -\frac{a_s A \delta_-}{s}\frac{i_{0,side}\alpha_{c,side}n_{side}F}{RT}\left(\frac{RT}{Fi_0(\alpha_a + \alpha_c)} - C_1 \frac{\frac{3}{FR_s} + \frac{2R_s s}{7D_s F}}{a_s\left(s + \frac{R_s^2 s^2}{35D_s}\right)}\right) \tag{27}$$

$$\frac{R_{SEI}(s)}{J_n(s)} = \frac{1}{s}\frac{a_s}{k_{SEI}}\frac{\tilde{V}_{SEI}}{n_{side}F}\frac{i_{0,side}\alpha_{c,side}n_{side}F}{RT}\left(\frac{RT}{Fi_0(\alpha_a + \alpha_c)} - C_1 \frac{\frac{3}{FR_s} + \frac{2R_s s}{7D_s F}}{a_s\left(s + \frac{R_s^2 s^2}{35D_s}\right)}\right) \tag{28}$$

$$\frac{\delta_{DL}(s)}{J_n(s)} = \frac{1}{s}\frac{\tilde{V}_{DL}}{n_{side}F}\frac{i_{0,side}\alpha_{c,side}n_{side}F}{RT}\left(\frac{RT}{Fi_0(\alpha_a + \alpha_c)} - C_1 \frac{\frac{3}{FR_s} + \frac{2R_s s}{7D_s F}}{a_s\left(s + \frac{R_s^2 s^2}{35D_s}\right)}\right) \tag{29}$$

The electrochemical model parameters in this study are listed in Table 1. To verify the aging model and parameters listed in Table 1, the comprehensive experimental setups are required to be carefully designed and introduced.

## 3. Experimental setup

### 3.1. Cycling tests

The lithium-ion cells used in this study are the commercial 18,650 cylindrical cells with 3.12 Ah nominal capacity. Anodes and cathodes of the cells consist of graphite and NCA, respectively. The cell voltage range is 2.5–4.2 V. The 18,650-type cells are placed inside the thermal chamber at an ambient temperature of 25 °C. The standard constant current/constant voltage (CC-CV) charging protocols followed by a 3C discharge are used to cycle the battery. In CC-CV stage, the cells were charged at a constant current until a cell voltage of 4.2 V is reached followed by a constant voltage phase until the current drops below 0.15A (0.05C). For every cycle, the battery is rested for 10 min between being charged and discharged. The discharge capacity is measured every 20 cycles via 1C discharge. The charge throughput during the 1C discharge process is defined as the capacity of the battery. Four cells corresponding to 1C CC-CV cycle, 2C CC-CV cycle, and 3C CC-CV cycle, respectively, are investigated in this study. The cycling test stops until the cycle number reaches 400. After 400 cycles, the relative capacity for 1C, 2C, and 3C drop to 74.8%, 71.8%, and 64%, respectively.

### 3.2. Electrochemical impedance spectroscopy (EIS)

After the cycling tests, the aged cells at 50% SOC are sent to the EIS test station to measure their impedance spectra. The measurements are performed in galvanostatic mode with 0.5A perturbation amplitude inside 10,000–0.1 Hz frequency range. Impedance spectra are tested for the fresh and cycled cells.

### 3.3. Post-mortem analysis

The discharged full cells were disassembled in the glove box filled with argon. The electrodes were studied visually both in a macroscopic and microscopic scale. Samples were taken from the electrodes and washed clearly with dimethyl carbonate (DMC) to remove the electrolyte salt residues. In addition to morphological analysis, the components of the aged electrodes are investigated by X-ray photoelectron spectroscopy (XPS) and X-ray diffraction (XRD) analysis. The flow chart shown in Fig. 2 summarizes the procedures of testing.

## 4. Experimental validation at macroscopic & microscopic levels

### 4.1. Voltage behavior examination

All the simulations are performed with SIMULINK in MATLAB. The cycle number 60, 220, and 340 are chosen to evaluate the cell's output responses at different aging status. The aging representatives are calculated online to update the model parameters periodically based on Eq. (30)–(32). Extra 1C discharge-resting-charge cycles are applied to test the battery's capacity in every 20 cycles. To validate the effectiveness of the proposed electrochemical aging model, the current curves during 1C capacity tests under 1C, 2C, and 3C cycling conditions are used as input to benchmark the battery model. Fig. 3 compares the voltage response of the experiments and model simulation as a function of charging C-rates. The electrochemical aging model fits the experimental results very well during most of the operating range. As the cycle number increases, the cell voltage decreases and the discharge duration become shorter as a result of capacity decay. The RMS error of voltage response with 1C, 2C, and 3C charging C-rates after different cycles are summarized in Table 2. After 340 cycles, the RMS error at 1C, 2C,

**Table 1**
Electrochemical parameters of the 18,650 NCM battery.

| Symbol | Units | Negative | Separator | Positive |
|---|---|---|---|---|
| $\mathbf{D_s}$ | $m^2s^{-1}$ | $3.7 \times 10^{-13}$ | | $9.9 \times 10^{-9}$ |
| $\mathbf{D_e}$ | $m^2s^{-1}$ | $2.25 \times 10^{-12}$ | $4.2165 \times 10^{-11}$ | $2.08 \times 10^{-11}$ |
| **L** | m | $9 \times 10^{-5}$ | $1.5 \times 10^{-5}$ | $6 \times 10^{-5}$ |
| **R** | m | $8 \times 10^{-6}$ | | $9 \times 10^{-6}$ |
| **A** | $m^2$ | 0.0779 | 0.0779 | 0.0779 |
| κ | $S\ m^{-1}$ | 1.7626 | 0.0779 | 0.0779 |
| εs | | 0.356 | | 0.3 |
| εe | | 0.3653 | 0.5 | 0.3653 |
| t+0 | | 0.363 | 0.363 | 0.363 |
| $\mathbf{C_{s,\ max}}$ | $mol\ m^{-3}$ | $25.6 \times 10^4$ | | $28.2 \times 10^4$ |
| $\mathbf{C_{e,0}}$ | $mol\ m^{-3}$ | 1200 | 1200 | 1200 |
| α | | 0.5 | | 0.5 |
| **k** | $mol^{-1/2}m^{5/2}\ s^{-1}$ | $5.39 \times 10^{-12}$ | | $2.31 \times 10^{-11}$ |
| **Stoichiometry at 0% SOC** | | 0.03 | | 0.7136 |
| **Stoichiometry at 100% SOC** | | 0.39 | | 0.3612 |
| $\tilde{V}_e$ | $m^3mol^{-1}$ | 1.8 | | |
| $\tilde{V}_{SEI}$ | $m^3mol^{-1}$ | $2 \times 10^{-5}$ | | |
| $\tilde{V}_{DL}$ | $m^3mol^{-1}$ | $4.14 \times 10^{-4}$ | | |
| $U^{\theta}_{eq,side}$ | | 0.21 | | |
| $\kappa_{SEI}$ | $S\ m^{-1}$ | $2 \times 10^{-5}$ | | |
| $\kappa_{DL}$ | $S\ m^{-1}$ | $1.89 \times 10^{-5}$ | | |
| $i_{0,side}$ | $Am^{-2}$ | $0.55 \times 10^{-5}$ | | |
| $\alpha_{c,side}$ | | 0.7 | | |
| $\alpha_{iso}$ | | 0.75 | | |
| $n_{side}$ | | 2 | | |

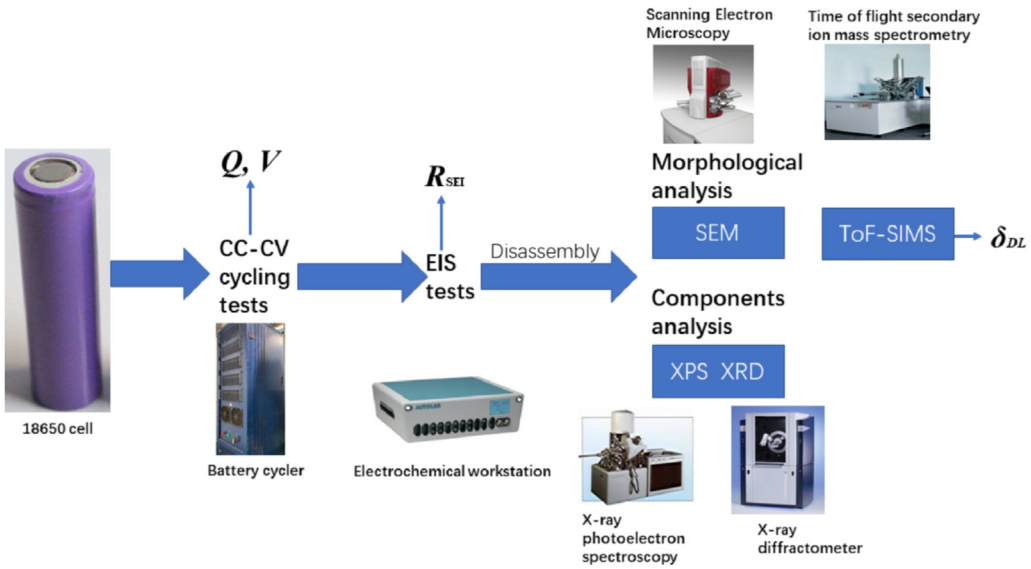


**Fig. 2.** Flow chart of experiment.

and 3C are 36.3 mV, 39.5 mV, and 42.0 mV, respectively. The results show that the aging model could maintain sufficient accuracy in terms of voltage response prediction [4].

### 4.2. Capacity fade

The capacity drop could be mainly resulted from the electrolyte depletion and massive loss of Lithium ions caused by the side reactions [23]. Therefore, the loss of electrolyte solvent and the decrease of initial anode SOC are considered as key parameters to reformulate the accurate cycle life model. The loss of electrolyte solvent $\Delta\varepsilon_e$ consumed by side reactions is modelled using the volume fraction of electrolyte as follows:

$$\Delta\varepsilon_e = -\frac{\alpha\tilde{V}_e Q_{ionloss}}{A\delta_- F} \tag{30}$$

where $\alpha$ is assumed to be 1 in this paper, indicating that 1 mol of electrolyte is consumed when 1 mol of lithium ion is consumed. $\tilde{V}_e$ is the molar volume of electrolyte. In addition, the newly-formed layer produced by the side reactions could isolate some particles, leading to the loss of active materials, which plays a significant role in capacity modelling and should be considered [10]. This phenomenon is described as:

$$\Delta\varepsilon_s = \delta_{DL} a_s \alpha_{iso} \tag{31}$$

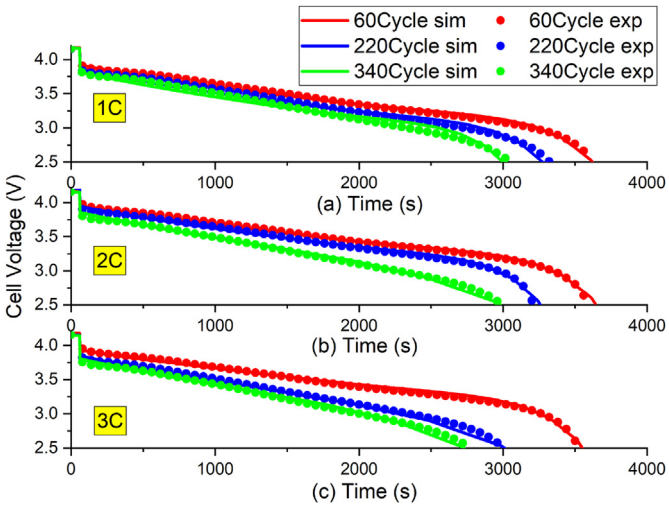


**Fig. 3.** 1C discharge characteristics of the degraded cells after different cycles at 1C CCCV (a), 2C CCCV (b), and 3C CCCV cycles (c).

**Table 2**
Voltage RMS error (mV) with 1C, 2C, and 3C charging C-rates.

| | 1C | 2C | 3C |
|---|---|---|---|
| 60 cycles | 24.6 | 27.8 | 29.7 |
| 220 cycles | 31.0 | 32.7 | 35.2 |
| 340 cycles | 36.3 | 39.5 | 42.0 |

where $\alpha_{iso}$ is a dimensionless coefficient representing that the isolation rate from the side reactions. The initial anode SOC (stoichiometric number) is reduced due to the loss of ions caused by the side reactions and the effect can be calculated as [7]:

$$\Delta soc_n = \frac{Q_{ionloss}}{\varepsilon_s \delta_- A c_{s,\max,n} F} \tag{32}$$

The loss of ions, decrease of the volume fraction of electrolyte and active materials at the anode/separator interphase, and the increase of resistance of SEI and deposited layer after different number of cycles at 3C charge C-rate are calculated and plotted in Fig. 4. It can be noted in Fig. 4a that the loss of ions increase in the cycling process because of the consumption by the side reactions. Meanwhile, the electrolyte, as one of the reactants, is consumed continuously leading to the decrease of electrolyte volume fraction as shown in Fig. 4b. After 400 cycles, $\varepsilon_e$ of the cell with 3C charging C-rate near the anode/separator interface becomes 0.248, indicating a great likelihood of the electrolyte exhaustion. The similar trend could be observed for the volume fraction of active material as shown in Fig. 4c. The reduction of $\varepsilon_s$ is mainly induced by the isolation from the growing film. These isolated particles are unable to take part in the electrochemical reactions and might detach from the current collector, leading to a severe capacity fade [10]. The other major cause of degradation is the impedance rise of SEI and deposited layer due to side reactions as is shown in Fig. 4d and e, respectively. The accumulating rate of deposit layer resistance could be described as:

$$\Delta R_{DL} = \frac{\delta_{DL}}{\kappa_{DL}} \tag{33}$$

where $\kappa_{DL}$ is the inonic conductivity of the deposited layer. The increased resistance could lead to serious capacity and power fade in the cycling process [22].

The simulated discharge capacity is obtained by updating the aforementioned degradation parameters at discharging with 1C rate for every 20 cycles at 25 °C. The detailed capacity decay modeling and calculation process can be referred in Ref. [10,29]. Experimentally measured and theoretically predicted discharge capacity versus number of cycles under four different charging C-rates are summarized in Fig. 5. The light blue area bounded by two red lines in the upper subplot of Fig. 5 denotes the absolute error range (±3%). The numerical results are found to match the experimental values reasonably well up to 400 cycles. It is noted that more severe degradation is observed and predicted at higher charging C-rates. The side reaction rate with high C-rates could be more aggressive, which could result in intensive consumption of ions, electrolyte, and active materials [5]. As is shown in Fig. 5d, the absolute error of the simulated values are maintained below 3%, which demonstrates the aging model is able to predict the capacity decay over the battery lifespan [4].

### 4.3. Resistance increase-electrochemical impedance spectroscopy analysis

The impedance spectra under different C-rates at the 0$^{th}$, 200th and 400th cycle are plotted in Fig. 6a, c and e as Nyquist plots (*-Im* (Z) vs. *Re* (Z)). The shapes of the measured spectra differ, showing one semi-circle (fresh, 1C, and 2C) or two partly overlapping semi-circles (3C). In general, the semi-circles in Nyquist plots are determined by the electrochemical processes at electrodes. To evaluate the impedance clearly, an equivalent circuit model (2nd RC) for EIS fitting is utilized to extract a set of electrochemical parameters as shown in Fig. 6b, d and f [13,34]. The cell's ohmic resistance ($R_o$) caused by electrolyte, separator, current collector and electrode equals to the spectrum's high frequency intercept with *Re*(Z) axis. $R_1$ and $C_1$ represent SEI resistance and capacitance at anode, respectively, which control the shape of the first semi-circle. $R_2$ and $C_2$ are charge transfer resistance and double layer capacity, respectively. They dominate the shape of the second semi-circle [7]. The SEI growth is considered as one of the most relevant parameters to battery aging in this paper, therefore, it is extracted and plotted in Fig. 6b–d together with the simulated SEI resistance values. It is observed that the simulation results tend to follow the experimental data with some deviations. Generally, the SEI resistance resulted from the accumulated side reaction products increases more with higher C-rate.

The aforementioned three validation processes are based on the cell-level external dynamic response. To present a comprehensive verification of the proposed aging model, the cells are disassembled and investigated microscopically on morphologies and components.

### 4.4. Deposited layer quantification

To investigate the changes of material compositions and morphologies of the aged cells, the cycled cells are discharged and opened up. Macroscopic pictures of cathodes and anodes under 1C, 2C and 3C are listed in Fig. 7a. While the new cell shows homogeneous and smooth anode surfaces, the cycled anodes have a striking variation in appearance. There is no obvious visual change regarding the cathode surface taken from the aged cells. For all cycled negative electrodes, the detachment of graphite from the copper current collector can be observed. As explained previously,

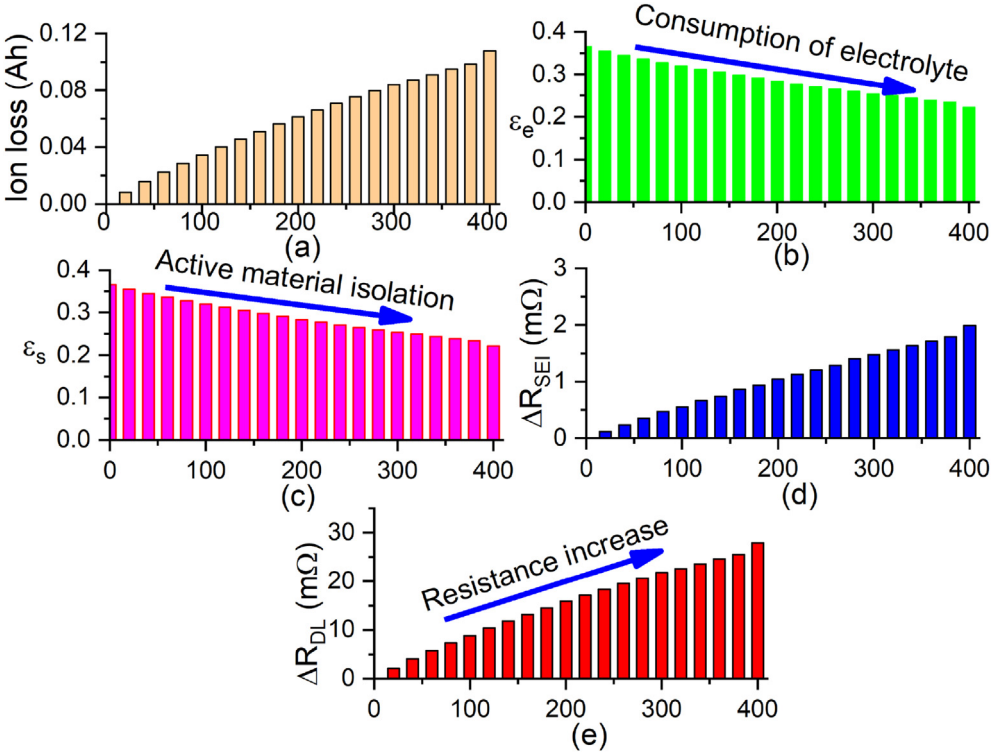


**Fig. 4.** Loss of ions (a), loss of active electrolyte (b), loss of active materials (c), and increase of SEI (d) and deposited layer resistance (e) with increased cycle number at 3C charging rate.

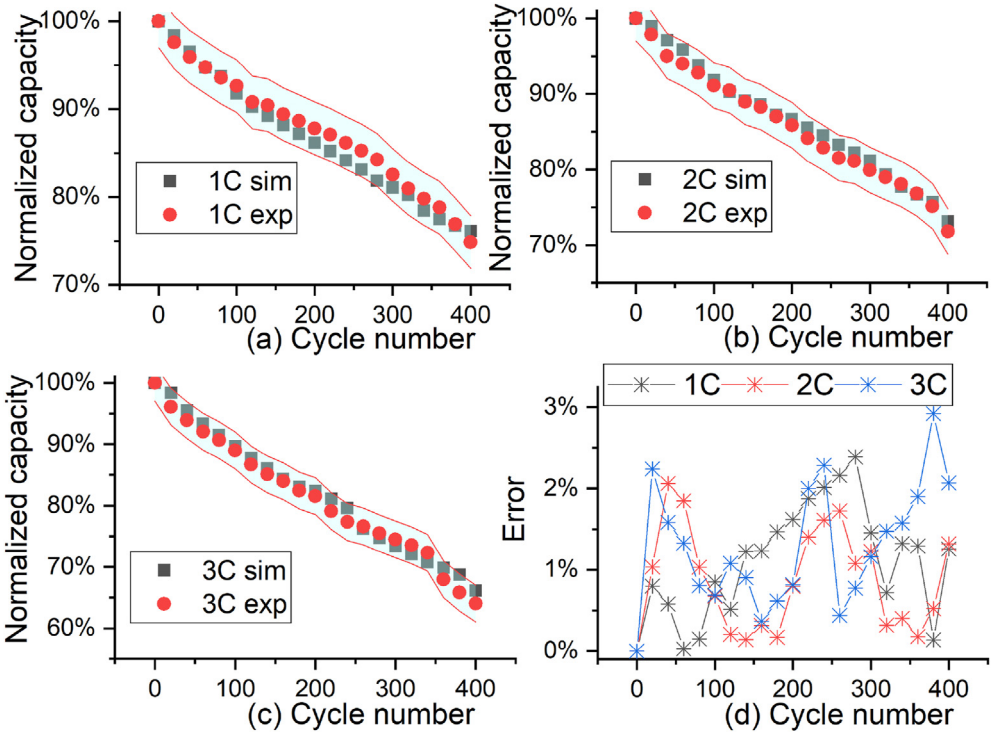


**Fig. 5.** Simulated and experimental capacity fade vs cycle number at 1C (a), 2C (b), 3C (c) charging C-rates, and the absolute simulation error (d).

the overgrowth of deposited layer can isolate some of the active particles and prevent them from intercalation or de-intercalation reactions. As a result, the loss of adhesion could occur [12]. Moreover, the cycled anode surfaces with 1C, 2C, and 3C are covered with a white light deposited layer, compared to the fresh anode. Scanning Electron Microscopy (SEM) is used to investigate

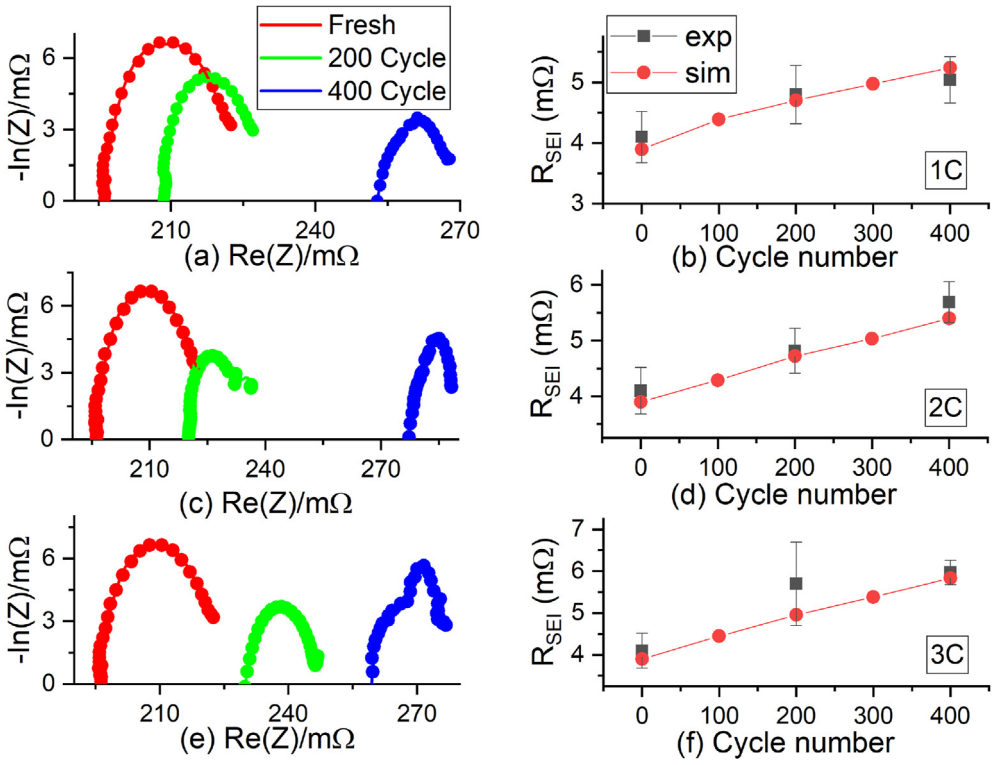


**Fig. 6.** Impedance characteristics measured by EIS, SEI resistance estimated by EIS and simulation results for new and aged cells after 400 cycles with 1C (a, b), 2C (c, d), and 3C (e, f) charging C-rates.

both the positive and negative electrodes microscopically. The SEM images of the fresh and degraded cells are shown in Fig. 7b. Some cracks are observed for the cathode particles of cycled cells compared to the fresh ones, which might be caused by the mechanical stress generated by the $Li^+$ diffusion in the electrode particles during charge and discharge [27]. In this paper, the cathode aging effects are neglected in the modeling and calculation process. The anode particles of the cycled cells are coated by distinct white deposits, which are dispersed randomly all over the carbon surface. It is evident that the coverage ratio of deposited layer changes with cycling C-rates and the cycled cell at 3C experiences the most serious degradation process. To quantify the severity of battery aging, the cross-section images of the anode electrodes taken by SEM integrated with TOF-SIMS are shown in Fig. 7. The color distribution represents the concentration of the elements. The bright-blue area represents the layered graphite particles cross-section parts. The red region means that Li is massively accumulated. The deeper the color demonstrates, the more concentration of Li element that exists in those place. As for the bright-red region as circuited in Fig. 7, it is assumed that Li is mostly deposited, which indicates the location and morphology of the deposited layer [40]. To obtain an unbiased evaluation of the thicknesses, over 50 measurements are carried out. Fig. 8 displays the distribution of the thickness of the deposited layer at 1C, 2C and 3C charging C-rates. Fig. 8a shows that $\delta_{DL}$ at 1C are in the range of 0.25 μm−1.83 μm. The curve in the histogram represents the probability of $\delta_{DL}$. Fig. 8b compares the distribution of $\delta_{DL}$ at 1C with a standard normally distributed data, and the result indicates that the $\delta_{DL}$ is almost normally distributed with 95% confidence intervals. For every cycling condition, over 50 samples are randomly measured, indicating that the tested $\delta_{DL}$ are not likely to include any outliers and the comparison among $\delta_{DL}$ with different charging C-rates are credible. Two key parameters of the normal distribution, which are the mean value (μ) and the variance (δ) of Fig. 8a−c are summarized and compared to the simulated values of $\delta_{DL}$ in Table 3. It is noted that all the simulated values of $\delta_{DL}$ at 1C, 2C, and 3C are within the '1-δ-interval' (μ-δ, μ+δ) as depicted in Fig. 8g, which mean that the simulation results are near the mean value. This illustrates that the calculated value is reliable in capturing the deposited layer growth inside the battery [35,36].

To identify the components of the deposited layer on the anode surface, X-ray diffraction (XRD) patterns for cathode and anode from fresh and degraded cells are shown in Fig. 9a−b. As it can be seen from Fig. 9a and b, almost all the diffraction peaks are overlapping, indicating that no new phase formation or obvious structure change can be detected both on the anode and cathode surface [28]. The surface compounds from fresh and aged cells under 3C are further investigated using XPS, spectrums from which are shown in Fig. 9c−d. The elements C, O, and Li are detected both on anodes and cathodes. However, it is to be noticed in Table 4 that the mass coefficient of O and Li at anode are almost two times larger than that at cathode. Thus, it can be concluded that the side reaction occurring at anode is the severest [29]. By examining the binding energies for Li1s, C1s and O1s at aged anodes and those characterized in $Li_2CO_3$ as summarized in Table 5, it is found that the deposited layer on anode surface should have a major component of $Li_2CO_3$, which mainly constitutes the SEI as well [30].

Based on the comparisons between aging model and experimental values, it is verified that the proposed battery aging model is capable of estimating the battery degradation over the battery

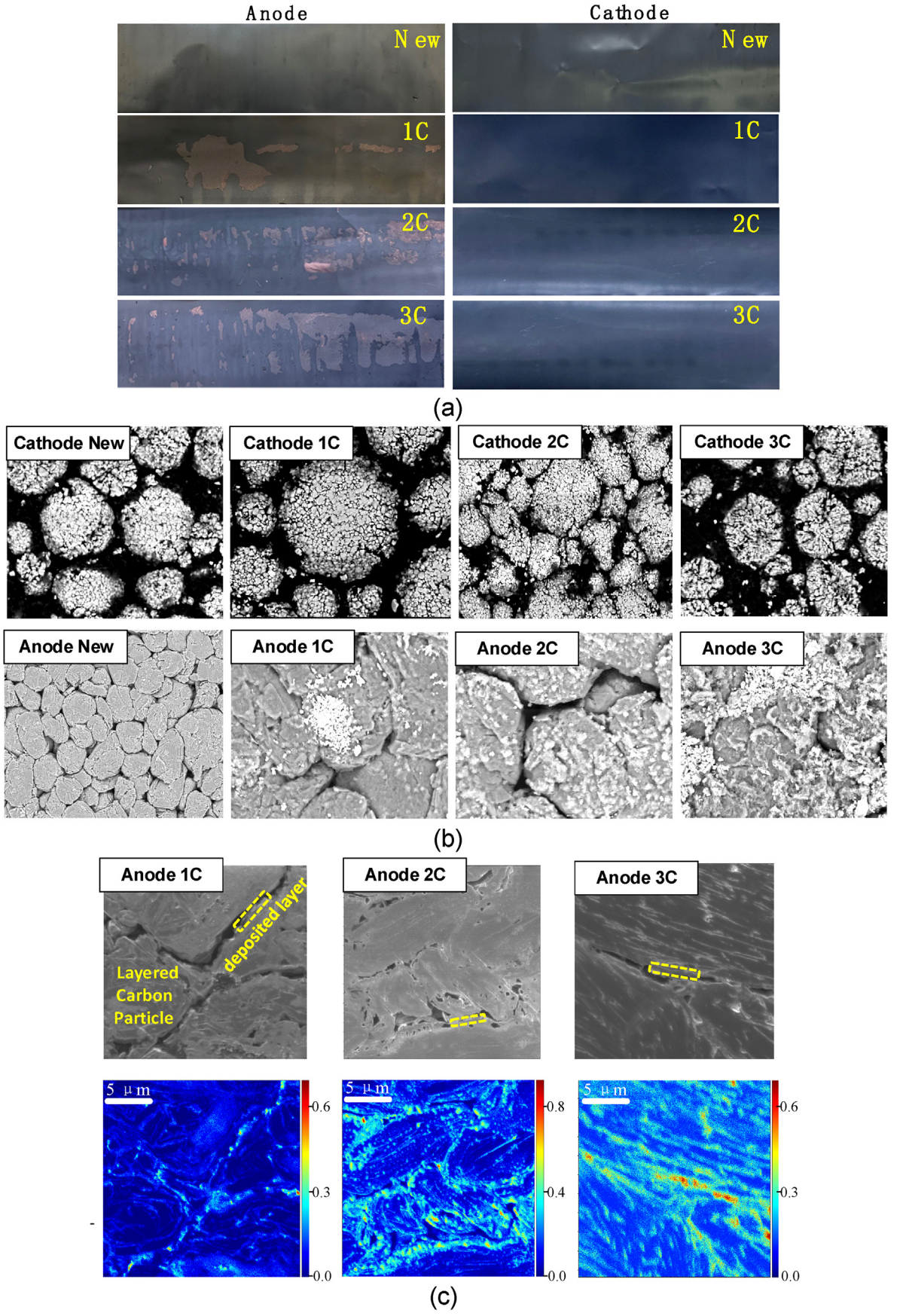


**Fig. 7.** Photographs of the anodes and the cathodes after 400 cycles (a), SEM pictures of anodes and cathodes surface (b), Cross-section pictures of aged anodes after 400 cycles with SEM (upper) and TOF- SIMS (below) (c).

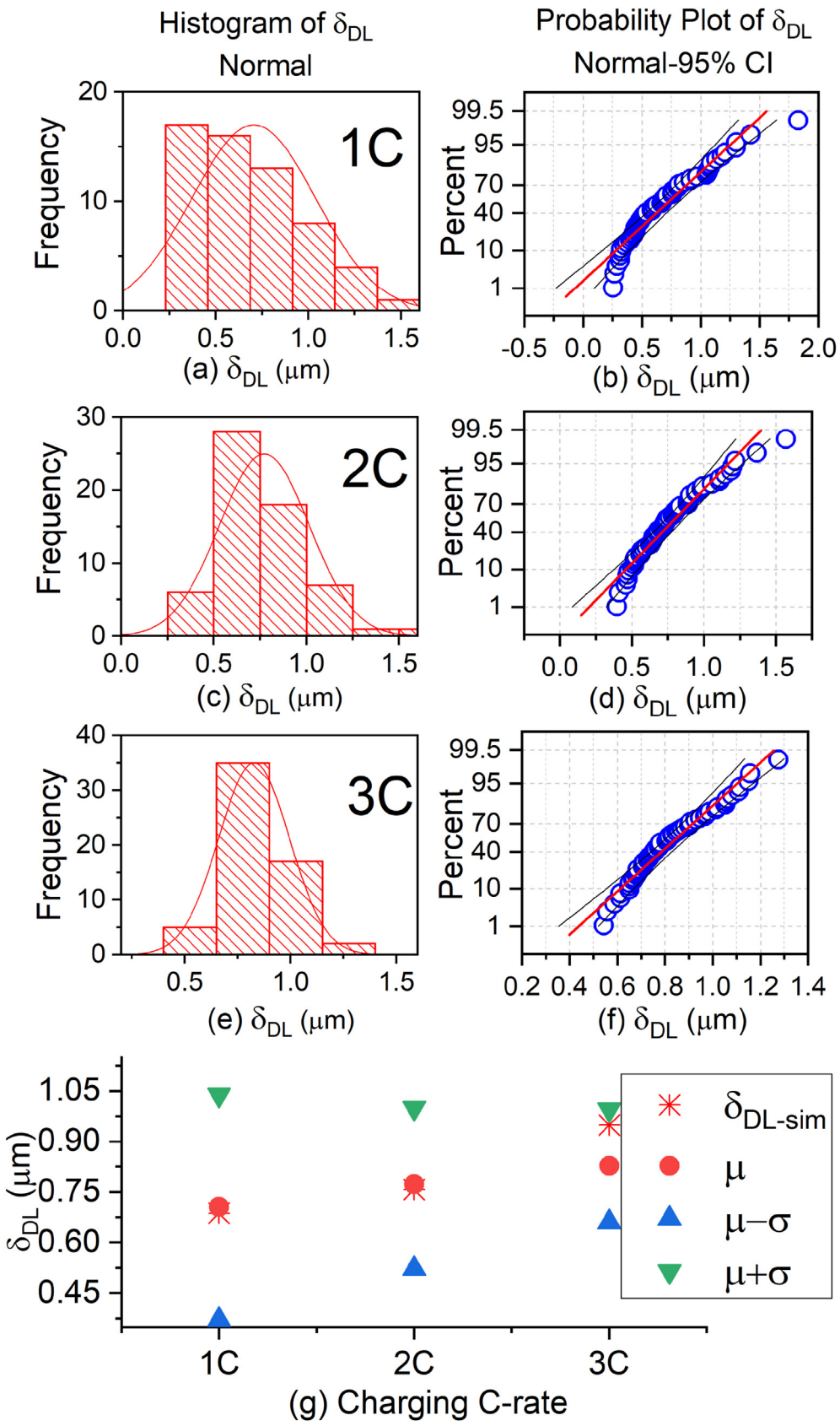


**Fig. 8.** Thickness of deposited layer of aged cells after 400 cycles with 1C (a, b), 2C (c, d) and 3C (e, f) charging C-rates, comparison of the thickness of the deposited layer between simulated values and measured values of aged cells after 400 cycles (g).

**Table 3**
Thickness of deposited layers on the anode particle surface.

| Charging C-rate | μ (μm) | δ (μm) | (μ-δ, μ+δ) | Simulated $\delta_{DL}$(μm) |
|---|---|---|---|---|
| 1C | 0.70523 | 0.33351 | (0.37172, 1.03874) | 0.68645 |
| 2C | 0.77259 | 0.24407 | (0.52158, 0.99942) | 0.75709 |
| 3C | 0.82756 | 0.16765 | (0.65991, 0.99521) | 0.94933 |

**Table 4**
Mass coefficient (%) of Li 1s and O 1s from anode and cathode surface.

| | Li 1s | | O 1s | |
|---|---|---|---|---|
| | Fresh | Aged at 3C | Fresh | Aged at 3C |
| Cathode | 8.44 | 10.91 | 15.76 | 18.59 |
| Anode | 17.52 | 20.58 | 24.58 | 30.37 |

**Table 5**
Binding energies(eV) for Li2CO3.

| Investigator | C1s | Li1s | O1s |
|---|---|---|---|
| Our work | 290.3 | 54.92 | 531.52 |
| Reference [7] | 289.8 | 55.23 | 531.73 |

lifespan. Since the aging model is based on the transfer-function relationship, it is easy to implement the model in Simulink. This is particularly useful, because the Simulink Coder can automatically produce embedded C and C++ code, which can be implemented in an embedded battery-management system (BMS) [31]. Therefore, the degradation aging model is very likely to be used for the real applications in evaluating the overall state-of-health of on-board batteries, including the capacity fade, resistance increase, loss of electrolyte solvent and active materials.

## 5. Conclusions

A novel electrochemical simplified aging model is proposed via solving for the transfer function between the aging representatives and input current. Three representative aging parameters are chosen to quantify the aging effects caused by battery side reactions, which are capacity loss, deposited layer growth and SEI resistance. Post-mortem analysis on material degradation of aged cells after 400 cycles using Electrochemical impedance spectroscopy, X-ray diffraction, X-ray photoelectron spectroscopy and Scanning electron microscopy have revealed that the side reactions at anode are the major cause for performance degradation. The side reactions lead to the overgrowth of solid-electrolyte interphase and produce an apparent deposited layer on the anode particle surface. Comparison with experimental voltage response of aged cells after 400 cycles shows that the reduced-order electrochemical aging model is able to operate up to 3C CCCV charge-3C discharge cycles. The capacity loss caused by side reactions and the deposited layer growth are predicted by the aging model and compared to the experimental results from 2 months of cycling tests with three different C-rates. The RMS voltage error is within 42 mV and the capacity decay error is bounded to 3%. The results demonstrate that aging model is successfully validated both at cell level and microscopic mechanism level. Besides, the proposed aging model provides significant insights into the battery degradation process. In the future, we will extend the simplified cell model to a pack-level and module-level at different driving conditions.

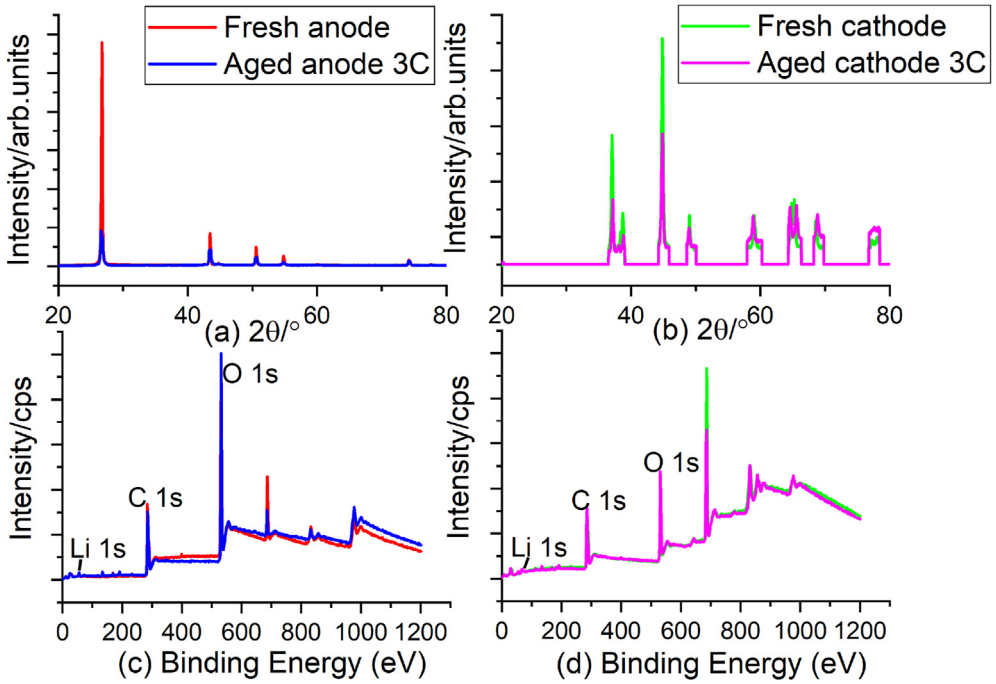


**Fig. 9.** XRD spectra of anodes (a) and cathodes (b) surface from new and aged cells at 3C after 400 cycles; XPS spectra of anodes (c) and cathodes (d) surface from new and aged cells at 3C.

## Declaration of competing interest

The authors declare that they have no known competing financial interests or personal relationships that could have appeared to influence the work reported in this paper.

## CRediT authorship contribution statement

**Xi Zhang:** Conceptualization, Funding acquisition, Methodology, Formal analysis, Writing - original draft. **Yizhao Gao:** Investigation, Methodology, Software, Validation, Visualization, Formal analysis, Writing - original draft. **Bangjun Guo:** Methodology, Writing - review & editing. **Chong Zhu:** Writing - review & editing. **Xuan Zhou:** Writing - review & editing. **Lin Wang:** Writing - review & editing. **Jianhua Cao:** Writing - review & editing.

## Acknowledgements

The authors gratefully acknowledge the support provided by the National Key R&D Plan Key Special Project (2017YFE0102000) and National Natural Science Foundation of China (NSFC) under the Grant number of 51677118.

## References

[1] Y. Wang, C. Zhang, Z. Chen, On-line battery state-of-charge estimation based on an integrated estimator, Appl. Energy 185 (2017) 2026–2032.
[2] S. Yang, Y. Hua, D. Qiao, Y. Lian, Y. Pan, Y. He, A coupled electrochemical-thermal-mechanical degradation modelling approach for lifetime assessment of lithium-ion batteries, Electrochim. Acta 326 (2019) 1–12.
[3] X. Tang, B. Liu, Z. Lv, F. Gao, Observer based battery SOC estimation: using multi-gain-switching approach, Appl. Energy 204 (2017) 1275–1283.
[4] R. Xiong, L. Li, Z. Li, Q. Yu, H. Mu, An electrochemical model based degradation state identification method of Lithium-ion battery for all-climate electric vehicles application, Appl. Energy 219 (2018) 264–275.
[5] M. Ouyang, X. Feng, X. Han, L. Lu, Z. Li, X. He, A dynamic capacity degradation model and its applications considering varying load for a large format Li-ion battery, Appl. Energy 165 (2016) 48–59.
[6] T.R. Tanim, C.D. Rahn, Aging formula for lithium ion batteries with solid electrolyte interphase layer growth, J. Power Sources 294 (2015) 239–247.
[7] R. Fu, S.-Y. Choe, V. Agubra, J. Fergus, Development of a physics-based degradation model for lithium ion polymer batteries considering side reactions, J. Power Sources 278 (2015) 506–521.
[8] J. Li, K. Adewuyi, N. Lotfi, R.G. Landers, J. Park, A single particle model with chemical/mechanical degradation physics for lithium ion battery State of Health (SOH) estimation, Appl. Energy 212 (2018) 1178–1190.
[9] R. Xiong, J. Tian, H. Mu, C. Wang, A systematic model-based degradation behavior recognition and health monitoring method for lithium-ion batteries, Appl. Energy 207 (2017) 372–383.
[10] R. Fu, S.-Y. Choe, V. Agubra, J. Fergus, Modeling of degradation effects considering side reactions for a pouch type Li-ion polymer battery with carbon anode, J. Power Sources 261 (2014) 120–135.
[11] M. Klett, R. Eriksson, J. Groot, P. Svens, K. Ciosek Högström, R.W. Lindström, H. Berg, T. Gustafson, G. Lindbergh, K. Edstorm, Non-uniform aging of cycled commercial LiFePO4//graphite cylindrical cells revealed by post-mortem analysis, J. Power Sources 257 (2014) 126–137.
[12] V.A. Agubra, J.W. Fergus, R. Fu, S.-Y. Choe, Analysis of effects of the state of charge on the formation and growth of the deposit layer on graphite electrode of pouch type lithium ion polymer batteries, J. Power Sources 270 (2014) 213–220.
[13] K. Jalkanen, J. Karppinen, L. Skogström, T. Laurila, M. Nisula, K. Vuorilehto, Cycle aging of commercial NMC/graphite pouch cells at different temperatures, Appl. Energy 154 (2015) 160–172.
[14] A. Schmidt, A. Smith, H. Ehrenberg, Power capability and cyclic aging of commercial, high power lithium ion battery cells with respect to different cell designs, J. Power Sources 425 (2019) 27–38.
[15] S. Phul, A. Deshpande, B. Krishnamurthy, A Mathematical model to study the effect of potential drop across the SEI layer on the capacity fading of a lithium ion battery, Electrochim. Acta 164 (2015) 281–287.
[16] S.K. Rahimian, S. Rayman, R.E. White, State of charge and loss of active material estimation of a lithium ion cell under low earth orbit condition using kalman filtering approaches, J. Electrochem. Soc. 159 (2012) A860–A872.
[17] X. Jin, A. Vora, V. Hoshing, T. Saha, G. Shaver, R.E. García, O. Wasynczuk, S. Varigonda, Physically-based reduced-order capacity loss model for graphite anodes in Li-ion battery cells, J. Power Sources 342 (2017) 750–761.
[18] E. Prada, D. Di Domenico, Y. Creff, J. Bernard, V. Sauvant-Moynot, F. Huet, A simplified electrochemical and thermal aging model of LiFePO4-graphite Li-ion batteries: power and capacity fade simulations, J. Electrochem. Soc. 160 (2013) A616–A628.
[19] A.V. Randall, R.D. Perkins, X. Zhang, G.L. Plett, Controls oriented reduced order modeling of solid-electrolyte interphase layer growth, J. Power Sources 209 (2012) 282–288.
[20] H. Ekstrom, G. Lindbergh, A model for predicting capacity fade due to SEI formation in a commercial graphite/LiFePO4 cell, J. Electrochem. Soc. 162 (2015) A1003–A1007.
[21] A. Jokar, B. Rajabloo, M. Désilets, M. Lacroix, Review of simplified Pseudo-two-Dimensional models of lithium-ion batteries, J. Power Sources 327 (2016) 44–55.
[22] X.-G. Yang, Y. Leng, G. Zhang, S. Ge, C.-Y. Wang, Modeling of lithium plating induced aging of lithium-ion batteries: transition from linear to nonlinear aging, J. Power Sources 360 (2017) 28–40.
[23] J. Park, W.A. Appiah, S. Byun, D. Jin, M.-H. Ryou, Y.M. Lee, Semi-empirical long-term cycle life model coupled with an electrolyte depletion function for large-format graphite/LiFePO 4 lithium-ion batteries, J. Power Sources 365 (2017) 257–265.
[24] T.R. Ashwin, Y.M. Chung, J. Wang, Capacity fade modelling of lithium-ion battery under cyclic loading conditions, J. Power Sources 328 (2016) 586–598.
[25] S. Yuan, L. Jiang, C. Yin, H. Wu, X. Zhang, A transfer function type of simplified electrochemical model with modified boundary conditions and Padé approximation for Li-ion battery: Part 1. lithium concentration estimation, J. Power Sources 352 (2017) 245–257.
[26] S. Yuan, L. Jiang, C. Yin, H. Wu, X. Zhang, A transfer function type of simplified electrochemical model with modified boundary conditions and Padé approximation for Li-ion battery: Part 2. Modeling and parameter estimation, J. Power Sources 352 (2017) 258–271.
[27] R. Fu, M. Xiao, S.-Y. Choe, Modeling, validation and analysis of mechanical stress generation and dimension changes of a pouch type high power Li-ion battery, J. Power Sources 224 (2013) 211–224.
[28] J. Zhu, X. Zhang, H. Luo, E. Sahraei, Investigation of the deformation mechanisms of lithium-ion battery components using in-situ micro tests, Appl. Energy 224 (2018) 251–266.
[29] Y. Gao, X. Zhang, J. Yang, B. Guo, Estimation of state-of-charge and state-of-health for lithium-ion degraded battery considering side reactions, J. Electrochem. Soc. 165 (2018) A4018–A4026.
[30] J. Vetter, P. Novák, M.R. Wagner, C. Veit, K.C. Möller, J.O. Besenhard, M. Winter, M.M. Wohlfahrt, C. Vogler, A. Hammouche, Ageing mechanisms in lithium-ion batteries, J. Power Sources 147 (2005) 269–281.
[31] J.R. Lee, L.L. Aldrich, K.D. Stetzel, G.L. Plett, Extended operating range for reduced-order model of lithium-ion cells, J. Power Sources 255 (2014) 85–100.
[32] L. Liu, J. Park, X. Lin, A.M. Sastry, W. Lu, A thermal-electrochemical model that gives spatial-dependent growth of solid electrolyte interphase in a Li-ion battery, J. Power Sources 268 (2014) 482–490.
[34] Y. Zhao, S. Choe, J. Kee, Modeling of degradation effects and its integration into electrochemical reduced order model for Li(MnNiCo)O2/Graphite polymer battery for real time applications, Electrochim. Acta 440 (2018) 440–452.
[35] G. Yang, J. Jinchun, Z. Caiping, Z. Weige, M. Zeyu, J. Yan, Lithium-ion battery aging mechanisms and life model under different charging stresses, J. Power Sources 356 (2017) 103–114.
[36] L. Xiao, L. Junran, M. Zhiqiang, L. Jun, Y. Hongyan, G. Haopeng, L. Gaoren, A method to determine nuclear magnetic resonance (NMR) T2cutoff based on normal distribution simulation in tight sandstone reservoirs, Fuel 225 (2018) 472–482.
[37] C. Zou, X. Hu, Z. Wei, T. Wik, B. Egardt, Electrochemical estimation and control for lithium-ion battery health-aware fast charging, IEEE Trans. Ind. Electron. 65 (8) (2018) 6635–6645.
[38] C. Wu, C. Zhu, Y. Ge, Y. Zhao, A review on fault mechanism and diagnosis approach for Li-ion batteries. A review on fault mechanism and diagnosis approach for Li-ion batteries, J. Nanomater. 2015 (2015) 1–9.
[39] A.U. Farmann, D. Sauer, A comprehensive review of on-board State-of-Available-Power prediction techniques for lithium-ion batteries in electric vehicles, J. Power Sources 329 (2016) 123–137.
[40] H. Masuda, N. Ishida, Y. Ogata, D. Ito, D. Fujita, In situ visualization of Li concentration in all-solid-state lithium ion batteries using time-of-flight secondary ion mass spectrometry, J. Power Sources 400 (2018) 527–532.
[41] P. Alexander, Electrochemical Model-Based State of Charge and State of Health Estimation of Lithium-Ion Batteries, PhD dissertation, Dept. Mechan., Ohio State Univ., USA, 2015.

## Nomenclature

$A$: sandwich area of the cell($m^2$)
$\delta$: Thickness of negative electrode(m)
$t+0$: cation transference number
$Rs$: particle radius of active material(m)
$a_{s,i}$: specific surface area of electrode($m^{-1}$)
$D_s$: diffusion coefficient in the solid phase($m^2 s^{-1}$)
$c_s$: lithium concentration in the solid phase(mol $m^{-3}$)
$k$: reaction rate constant of electrode ($mol^{-1/2} m^{5/2} s^{-1}$)
$\alpha_a$: transfer coefficient for anode reaction

$\phi$: potential in the electrolyte
$\bar{V}_{SEI}$: molar volume of SEI
$j_{side}$: current density of side reactions
$R_{SEI}$: resistance of SEI
$R$: universal gas constant (8.3143j $mol^{-1}k^{-1}$) or resistance
$F$: faraday constant(96487c $mol^{-1}$)
$L$: length between cu collector and al collector(m)
$\varepsilon s$: volume fraction of solid phase
$\varepsilon e$: volume fraction of liquid phase
$D_e$: diffusion coefficient in the liquid phase($m^2s^{-1}$)
$c_e$: lithium concentration in the liquid phase (mol $m^{-3}$)
$\kappa$: ionic conductivity (s $m^{-1}$)
$\alpha_c$: transfer coefficient for cathode reaction
$Q$: capacity
$i_0$: exchange current density($Am^{-2}$)
$j_{\mathrm{int}}$: current density of intercalation reactions
$\delta_{DL}$: thickness of deposited layer(m)